Variation in Ion Acceleration Characteristics of the HERMeS Hall Thruster during Magnetic Optimization

IEPC-2019-713

Wensheng Huang[*], Hani Kamhawi[†], and Daniel A. Herman[‡]
National Aeronautics and Space Administration Glenn Research Center, Cleveland, OH, 44135, USA

To reduce design risks for future magnetically shielded Hall thrusters, a test was performed on the HERMeS to obtain data for optimizing the effect of magnetic shielding. As a part of this test, laser-induced fluorescence velocimetry was used to characterize the variations in the ion acceleration with different magnetic configurations. Four magnetic configurations representing varying amounts of magnetic shielding between the high-energy discharge plasma and the discharge channel walls were tested. The ion velocity data points to the possibility that different plasma-wall interaction physics applies to a magnetically shielded thruster than a non-shielded thruster. The transition point is very prominent and can potentially be used to test whether a thruster is fully magnetically shielded.

Abbreviations

AEPS	=	Advanced Electric Propulsion System	MCD	=	Mean Channel Diameter
EDU	=	Engineering Development Unit	RFC	=	Reference Firing Condition
GRC	=	Glenn Research Center	SEP	=	Solar Electric Propulsion
HERMeS	=	Hall Effect Rocket with Magnetic Shielding	STMD	=	Space Technology Mission Directorate
			TDM	=	Technology Demonstration Mission
IPS	=	Ion Propulsion System	TDU	=	Technology Development Unit
JPL	=	Jet Propulsion Laboratory	VF	=	Vacuum Facility
LIF	=	Laser-Induced Fluorescence	WT	=	Wear Test

I. Introduction

FOR missions beyond low Earth orbit, spacecraft size and mass can be dominated by onboard chemical propulsion systems and propellants that may constitute more than 50 percent of spacecraft mass. This impact can be substantially reduced through the utilization of Solar Electric Propulsion (SEP) due to its substantially higher specific impulse. Studies performed for NASA's Human Exploration and Operations Mission Directorate (HEOMD) and Science Mission Directorate have demonstrated that a 40 kW-class SEP capability can be enabling for both near term and future architectures and science missions.[1]

Since 2012 NASA has been developing a 14-kW Hall thruster electric propulsion string that can serve as the building block for realizing a 40-kW-class SEP capability. NASA continues to evolve a human exploration approach to expand human presence beyond low-Earth orbit and to do so, where practical, in a manner involving international, academic, and industry partners.[2] NASA publicly presented a phased exploration concept at the HEOMD Committee of the NASA Advisory Council meeting on March 2017.[3] NASA presented an evolutionary human exploration architecture, depicted in Fig. 1, to expand human presence deeper into the solar system through a

---

[*] Ion Propulsion System Diagnostics Lead, EP Systems Branch, wensheng.huang@nasa.gov.
[†] Ion Propulsion System Test Lead, EP Systems Branch, hani.kamhawi-1@nasa.gov.
[‡] Ion Propulsion System Lead, EP Systems Branch, daniel.a.herman@nasa.gov.

phased approach including cis-lunar flight testing and validation of exploration capability before crewed missions beyond the Earth-Moon system and eventual crewed Mars missions. One of the key objectives is to achieve human exploration of Mars and beyond through the prioritization of those technologies and capabilities best suited for such a mission in accordance with the stepping stone approach to exploration.[4] High-power solar electric propulsion is one of those key technologies that has been prioritized because of its significant exploration benefits. A high-power, 40 kW-class Hall thruster propulsion system provides significant capability and represents, along with flexible blanket solar array technology, a readily scalable technology with a clear path to much higher power systems.
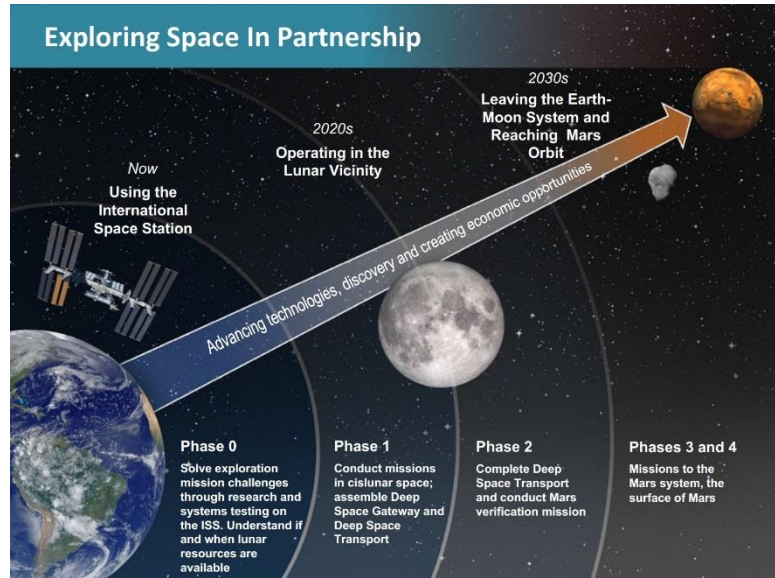

Figure 1. Deep Space Gateway and Transport Plan depiction.[5]

The 14-kW Hall thruster system development, led by the NASA Glenn Research Center (GRC) and the Jet Propulsion Laboratory (JPL), began with maturation of the high-power Hall thruster and power processing unit. In particular, the Hall thruster is called Hall Effect Rocket with Magnetic Shielding (HERMeS) Technology Development Unit (TDU). The technology development work has transitioned to Aerojet Rocketdyne via a competitive procurement selection for the Advanced Electric Propulsion System (AEPS). The AEPS contract includes the development, qualification, and production of multiple flight 14-kW electric propulsion string deliveries. The AEPS Electric Propulsion string consists of the Hall thruster, power processing unit (including digital control and interface functionality), xenon flow controller, and associated intra-string harnesses. During the development phase of the AEPS, Engineering Test Unit (ETU) Hall thrusters are being produced for testing.

To minimize technical risks associated with EDU development, the NASA team is performing risk reduction activities on the HERMeS TDUs.[6, 7] The specifications for the 12.5-kW HERMeS are enhanced compared to the current state of the art.[6] Characteristics of the thruster include high system efficiency ($\geq$57%), high specific impulse (up to 3000 s), and high propellant throughput capability (3400 kg). Additionally, HERMeS was designed to deliver similar system efficiency at a more modest specific impulse of 2000 seconds. High specific impulse operation supports mission concepts with high total-impulse requirements like deep-space exploration missions, while the modest specific impulse operation is beneficial for time-critical operations like LEO to GEO orbit raising.

A series of tests were performed on three HERMeS TDUs.[7] Figure 2 shows a diagram of the testing on the HERMeS TDUs thus far. ETU testing is scheduled to begin after the testing shown in this figure. Testing on the TDU1 included the propellant uniformity test,[8] magnetic shielding characterization test,[9] performance characterization test (PCT),[10-12] thermal characterization test (TCT),[13, 14] facility effect characterization test (FECT),[10, 12, 15] and the first wear test (WT) campaign. The PCT, TCT, and FECT were performed with a single test setup. The first wear test campaign, completed in 2016, included the electrical configuration characterization test (ECCT),[16, 17] two short duration tests,[18] and a long duration wear test.[17, 18] TDU1 was then used in a number of short duration wear tests[19] (part of the second wear test campaign), laser-

Figure 2. A diagram of the TDU test campaigns.

induced fluorescence (LIF) functional checkout test,[20, 21] and magnetic optimization test.[22] TDU2 underwent the acceleration zone characterization test,[23] pole erosion characterization test,[24] environmental test campaign,[25] and
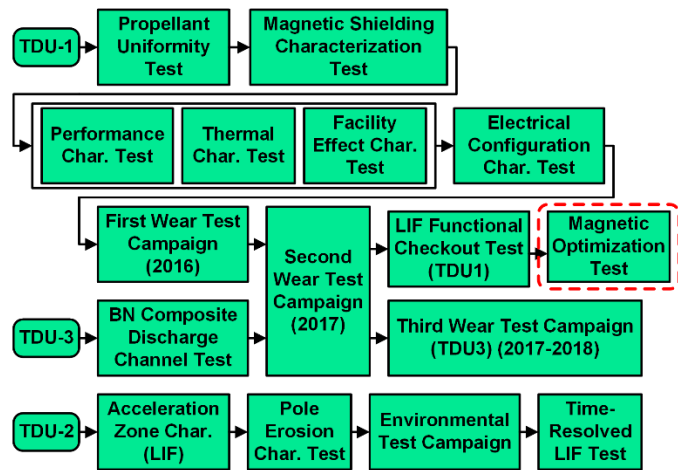
time-resolved LIF test.[26] TDU3 was used in another performance characterization test, which involved boron nitride composite discharge channel,[27] the second wear test campaign,[19] and the third wear test campaign.[28, 29] The third wear test campaign included a long duration wear test of the TDU3.[29] The bulk of this article is focused on the findings from the LIF portion of the magnetic optimization test performed on TDU1.

To reduce design risks for future magnetically shielded Hall thrusters, the magnetic optimization test was performed on the HERMeS to obtain data for optimizing the effect of magnetic shielding. As a part of this test, LIF velocimetry was used to characterize the variations in the ion characteristics with different magnetic configurations. Four magnetic configurations representing varying amounts of magnetic shielding between the high-energy discharge plasma and the discharge channel walls were tested. These four configurations were labeled B0, B1, B2, and B4 with B0 being the baseline configuration for the HERMeS TDU. B0 represented the most shielded configuration while B4 represented the least shielded configuration. The location of maximum radial magnetic field along channel centerline shifted upstream by approximately the same amount between each configuration to the next configuration in the sequence. For example, the shift axially along the channel centerline was twice as large between B2 and B0 versus B1 and B0. The shift between B4 and B0 was three times as large as the shift between B1 and B0.[22] Additional information regarding the differences between the configurations can be found in Kamhawi, et al.[22]

LIF velocimetry was deployed to examine the change in the acceleration zone, ion direction of travel, and energy of the ions bombarding the poles of the thruster between configurations. In particular, an analysis method that accounts for the Zeeman Effect was deployed and two ion populations near the inner front pole were individually characterized. One ion population appeared to originate from the discharge channel while the other appeared to originate from the cathode. Data was obtained for discharge voltages of 300 V and 600 V at nominal reference magnetic field strength. The reference magnetic field strength is the maximum radial magnetic field along the discharge channel centerline. Interrogation zones included inside the discharge channel, in the near-field of the channel exit, and downstream of the pole covers. This article will describe the experimental setup, data analysis, and results from the LIF portion of the magnetic optimization test.

Table 1. Table of Reference Firing Conditions.

Label	Discharge voltage, V	Discharge power, kW
300-2.7	300	2.70
*300-6.3	300	6.25
400-8.3	400	8.33
500-10.4	500	10.42
*600-12.5	600	12.50
630-13.1	630	13.12

*RFCs that were the focus of the testing described in this paper.

II. Experimental Setup

To simplify plot labeling, throttle points are labeled by discharge voltage, discharge power, and configuration number. A label that says "300-6.3-B0" refers to the throttle point with a discharge voltage of 300 V, a discharge power of 6.3 kW, and a magnetic field configuration of B0.

Unless otherwise noted, all spatial positions around the thruster are normalized based on the region of interest. For all regions, $Z = 0$ at the exit plane, which is defined by the inner front pole cover downstream surface, and Z is positive in the downstream direction. In the thruster discharge channel, radial positions are normalized by the discharge channel width, where $R = 0$ at the inner wall, $R = 1$ at the outer wall. Similarly, data near the inner and outer front pole covers are normalized so that $R = 0$ and $R = 1$ correspond to the inner and outer radial edges, respectively, of the region of interest.
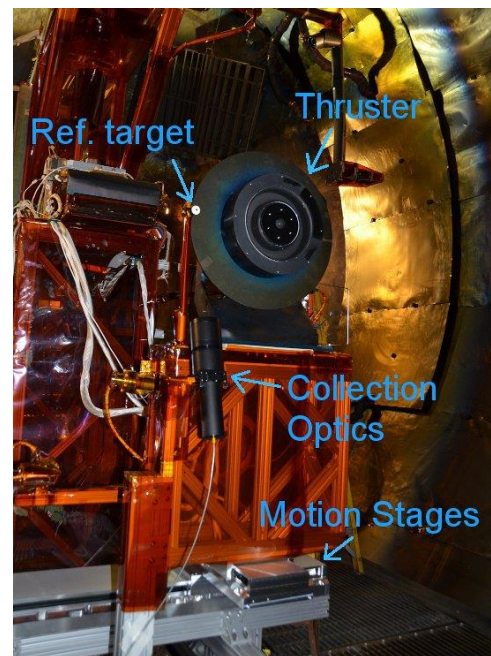
A. Thruster and Test Matrix

All data presented in this work were collected with the HERMeS TDU1. The HERMeS TDU was designed to be a 12.5 kW, 3000 s, magnetically-shielded Hall thruster. The thruster had been operated over discharge voltages ranging from 300 to 800 V, corresponding to a specific impulse range of 2000 to 3000 s at full power. The thruster had also been throttled over discharge powers ranging from 0.6 to 12.5 kW.[10] The cathode mass flow rate was maintained at 7% of the anode mass flow rate.

Peak radial magnetic field strength along the discharge channel centerline was chosen as the reference when referring to the strength

Figure 3. NASA HERMeS TDU1 and thrust stand setup.

of the magnetic field. A single magnetic field strength value was chosen as the nominal value for all operating conditions. Figure 3 shows a picture of the NASA HERMeS TDU1 on the LIF test stand.

The specifications for the TDUs included seven Reference Firing Conditions (RFCs), which were throttle points that would be used in all TDU testing. Though the full operational range of the TDUs extends well beyond the RFCs, testing was constrained to the RFCs to ensure consistency across tests and limit testing cost. Table 1 lists the RFCs. The testing described in this paper focused on two of the RFCs, which are marked with asterisks.

For the testing described in this paper, the thruster body was isolated from the test stand and connected to the cathode. Prior testing had determined that this cathode-tied configuration was associated with low pole cover erosion and can be readily implemented in flight.[16, 17]

Prior to testing in the B1, B2, and B4 configurations, thruster telemetry obtained during B0 testing was compared with prior TDU1 testing in Vacuum Facility 6 to confirm nominal thruster operations.[30]

B. Test Facility

Testing was performed in Vacuum Facility 6 at NASA GRC. This cylindrical facility is 7.6 m in diameter, 27.6 m long, and was evacuated with a set of cryo-pumps. The thruster was mounted on a test stand that can be moved horizontally with two cross-mounted motion stages. Figure 3 shows the thruster mounted on the test stand. Also in the figure are the reference target used for laser alignment, the collection optics, and the motion stages that move the test stand. Propellant was delivered via stainless steel tubing bent into coils at strategic locations to allow full range of motion without causing plastic deformation to the tubing. The tubing was wrapped with heat tape for propellant line bake-out to ensure high-purity propellant delivery. The heat tape was removed after the bake-out.

Background pressure near the thruster was monitored with two ion gauges, which were calibrated on xenon against a spinning rotor gauge. Gauge readings were corrected for temperature and direction relative to background flux via methods described in Yim and Burt.[31] Uncertainty in the calculated pressure was dominated by plasma-induced noise, electronic noise, and uncertainties associated with correction method. Total uncertainty in pressure is estimated to be 10% to 15% of the reading. The background pressure near the thruster for the testing described in this paper was 1.2×10^{-5} Torr.

Research-grade xenon propellant was supplied via commercially available mass flow controllers to the thruster and cathode. These mass flow controllers were calibrated using research-grade xenon prior to testing. Typical uncertainty of measurement was ±1% of reading.

Electrical power was supplied to the thruster with commercially available power supplies. Separate power supplies supported the main discharge, cathode heater, keeper, inner magnet, and outer magnet. An electrical filter was placed between the thruster and the discharge power supply. All power supplies and the filter were located outside of the vacuum facility.

C. Diagnostics

The LIF velocimetry scheme used in the LIF functional checkout test excited the XEII 834.953 nm (vac) transition and collected fluorescence from the 542.066 nm (vac) transition. Figure 4 shows a diagram of the LIF scheme used. This singly-charged xenon ion transition has an unusually narrow hyperfine structure that cannot be easily resolved even when probed with special techniques.[32] In a previous study, the pi-polarized Zeeman Effect[§] for this transition was found to be negligible.[33] The implication of the prior work is that if pi-polarization can be maintained, the broadening in the VDF obtained in the discharge channel of a Hall thruster is at most 4-5%.[32] However, for the TDU and ETU, regions of interest included regions with high magnetic field strength and where the local directions of the magnetic field were often out of alignment with the polarization directions of the laser beams. Instead of trying to maintain pi-polarization in some regions but not others, the decision was made to set the polarization direction of both side injection axes so that those scans are always purely sigma-polarized. The Zeeman-broadened data would then be corrected in post processing using a simplified linear model developed by Huang in a prior work.[33] Polarization direction of the axial injection axis was set to allow pi-polarization throughout most of the discharge channel while accepting increased broadening in certain regions. Within these regions, VDF width data from the side injection axes were used instead.


[§] In Zeeman Effect, photons are considered to be pi-polarized if their polarization is parallel to the direction of the external magnetic field experienced by the interacting particle. Photons are considered to be sigma-polarized if their polarization is perpendicular to the direction of the external magnetic field. If the direction of polarization is in between, quantum physics can be used to determine the probability that a given photon will interact as if it were sigma versus pi-polarized. However, this is not a simple process. In Hall thruster LIF applications where Zeeman Effect is important, in-between polarization should be avoided in order to reduce uncertainty.

The laser used in this LIF test was a taper-amplified diode laser that output up to 500 mW at 835 nm. Wavelength was monitored via a Fizeau-type wavemeter and an optogalvanic cell. The laser beam entering the optogalvanic cell was mechanically chopped at ~1.6 kHz. The laser beam was also monitored with photodiode to track the variation in laser power. The laser beam was split into three branches. Each branch passed through an electro-optical modulator and was collimated into an optical fiber. A modulation frequency study showed that the signal-to-noise ratio (SNR) optimized at around 300 kHz to 350 kHz in modulation frequency.

Figure 5 shows a diagram of the optics setup inside the vacuum facility. Three sets of injection optics where deployed. The optical fibers from the air-side setup were sent to each of the three sets of injection optics. Each set of injection optics had two motors that allowed remote control of the tilt and pan. The optics on axis 1, the axial axis, was protected from most of the heat of the plasma by a shield. Additionally, the support structure for the axis 1 optics was equipped with an internal cooling line connected to a chiller. The thruster was mounted to the motion stages that provide radial and axial movements. A reference target was mounted at a known distance from the thruster in the same plane as the three injected laser beams. Two cameras monitored the positions of the injected laser beams relative to the reference target. The collection optics were mounted 70° out of the injection plane. An optical fiber carried fluorescence signal from the collection optics out of the vacuum facility. The spatial resolution of the measurements was limited by the beam waist of the injection beams and the viewing cone of the collection optics to approximately 1 mm in size.

The light from the collection optical fiber was collimated into a monochromator and sent to a photomultiplier. The photomultiplier current was converted to voltage via a high-speed trans-impedance amplifier. The output voltage signal was coupled into three digital lock-in amplifiers. A fourth digital lock-in amplifier measured the signal from the optogalvanic cell. A computer controlled the movement of various stages, swept the laser wavelength, and recorded the various output signals. Lock-in amplifier time constant varied from 300 ms to 1 s.
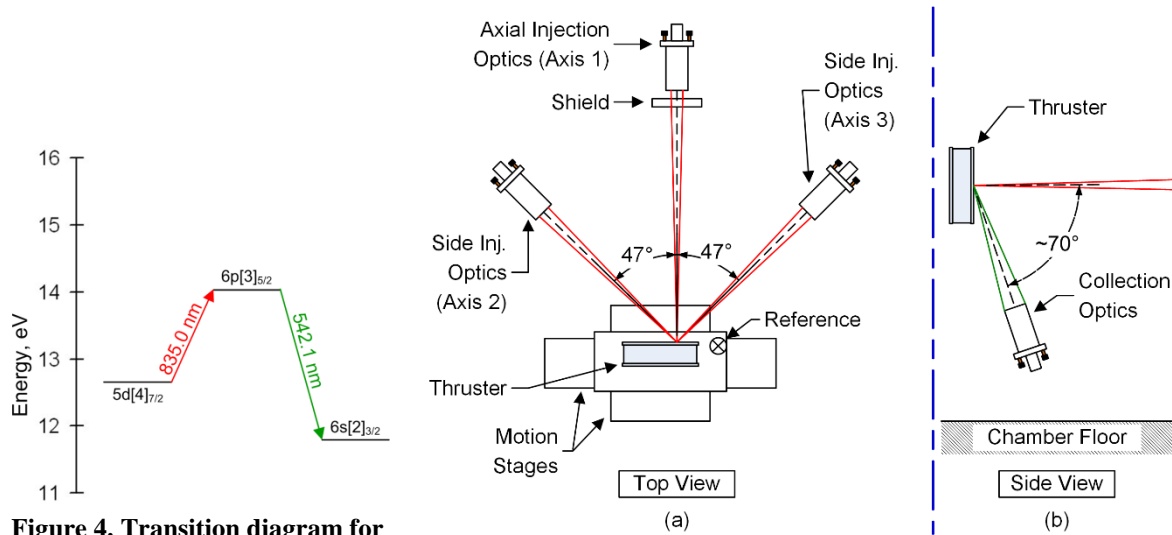
Figure 4. Transition diagram for Xe II LIF at 834.953 nm (vac).

Figure 5. Vacuum-side optical setup.

Due to the small size of the interrogation zone relative to the length scale of the rest of the vacuum facility, shifts in laser alignment over the course of the experiment can easily take the injected beams and the collection optics out of alignment if not corrected for. The LIF diagnostic system used a reference pin, a catcher disc, and two cameras to track the position of the laser beams relative to the thruster. Since the reference pin is 1 mm in diameter, change in alignment as small as 0.1 mm can be detected by observing the intensity of the laser light reflected off of the alignment pin. If the alignment drifted by more than 1 mm, the laser beams would fall on the catcher disc and could be seen in the cameras. The cameras had their IR-cut filters removed so that they could see the near-IR laser beam.

III.   Data Analysis

A. Analysis Method

A saturation study was performed at the beginning of the test campaign to pick out injection laser power that balances saturation broadening and SNR (i.e. high laser intensity leads to higher SNR but also more saturation broadening). The amount of broadening was kept to below 10%.

The first step in the data analysis was to convert readings from the wavemeter and optogalvanic cell into frequency shift from the stationary transition frequency. This frequency shift was sometimes referred to as the detuning. The detuning was then converted into a velocity scale.

The intensity data was corrected for changes in laser power by using a combination of photodiode and thermopile measurements. First, the laser power as measured by the thermopile and the photodiode were collected in a controlled study. Then, the photodiode measure during data acquisition was corrected by the results of the controlled study to provide an accurate measurement of the laser power. This correction removed artificial features that may have been created in the intensity data due to variations in laser power as the wavelength varied.

Next, curve-fits were performed on the intensity versus the velocity. Three different types of curve-fits were used including skew-normal, Gaussian, and Two-Gaussian

Figure 6. An example of skew-normal curve-fit.

Figure 7. An example of Two-Gaussian curve-fit.

functions. Figure 6 shows an example of skew-normal curve-fit. Figure 7 shows an example of Two-Gaussian curve-fit. Two-Gaussian fits were used when skew-normal and Gaussian distributions do not adequately capture the lineshape.

For the side injection axis, which were purely sigma-polarized, Zeeman Effect on the hyperfine structure was corrected by applying a simple linear model for the XEII 834.953 nm (vac) transition.[33] The model is reproduced here in the form of Eq. (1) for convenience.

$$Zeeman\ splitting\ in\ MHz = 2.7273 \times Magnetic\ field\ strength\ in\ Gauss \qquad (1)$$

To apply the model, magnetic field simulation of the TDU was used. This magnetic field simulation was validated using magnetic field measurements of the three TDUs. At each location where LIF data was taken, the magnetic field strength in the axial-radial plane was extracted from the simulation and inputted into Eq. (1). The resulting splitting amount was convoluted with the curve-fit and then compared to the lineshape. Once a set of acceptable curve-fit parameters were determined, the curve-fit without the Zeeman Effect was taken to be the final result of the Zeeman Effect correction. For a brief explanation of convolution, please see this prior work.[34] On average, the Zeeman Effect correction reduced the width of the VDFs by about 3-5%. However, in regions of high magnetic field, the correction reduced the width of the VDFs by as much as 40%.

Once the curve-fits were performed, averaged velocities and full-width-at-half-maximum (FWHM) velocities were calculated. If a Two-Gaussian fit was used, additional analyses were performed depending on the location associated with the data. For data found in the acceleration zone of the thruster, where large changes in velocity have been observed, the Two-Gaussian fits were analyzed as if they were a single population spread out by plasma potential oscillations. For data found near the discharge channel but downstream of the acceleration zone, the two peaks found were assumed to be two distinct populations. In such a case, the averaged energy and direction of the two peaks were separately calculated and the results compared to far-field retarding potential analyzer data to confirm that they were indeed two separate populations. A prior publication contains greater detail of how the low energy population was identified and speculated to be charge-exchange (CEX) ions.[20] For data found near the inner pole cover, the ions were analyzed as two distinct ion populations. Another prior publication describe how the two distinct ion populations were identified.[21]

B. Uncertainty Analysis

The uncertainty in position was dominated by the size of the interrogation zone and the drift in alignment of the optics. The alignment procedure used in this LIF test rejected data where alignment drifted by more than 0.5 mm from the reference.
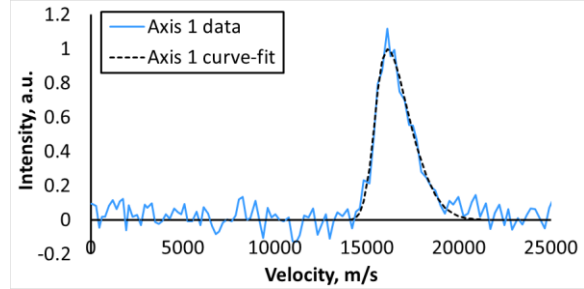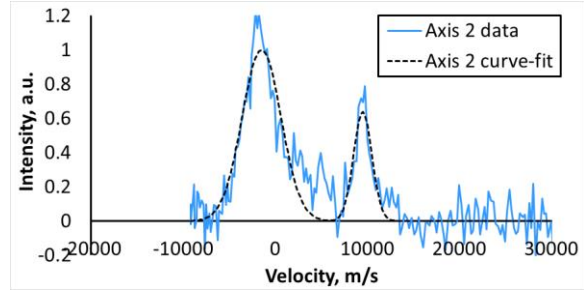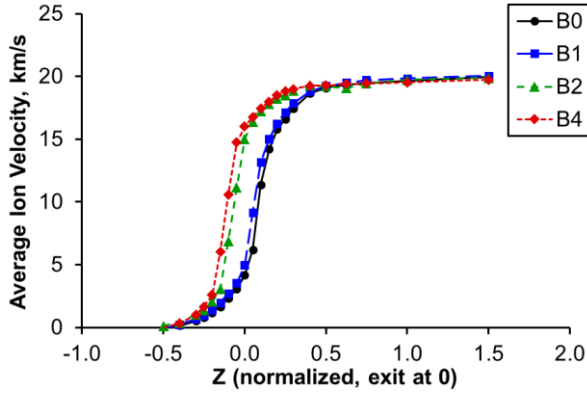
Figure 8. Averaged axial ion velocity along the discharge channel centerline for the TDU1 operating at 300 V, 6.3 kW with different magnetic field configurations.
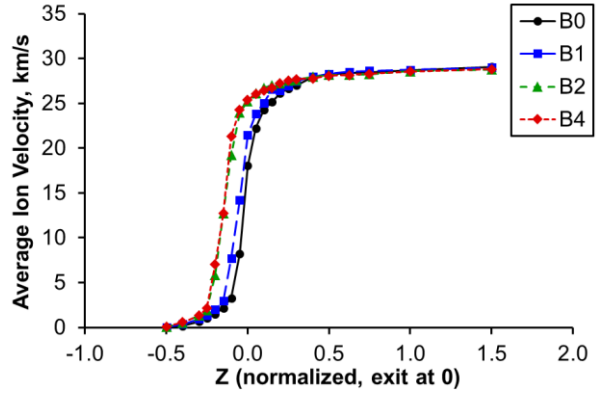

Figure 9. Averaged axial ion velocity along the discharge channel centerline for the TDU1 operating at 600 V, 12.5 kW with different magnetic field configurations.

The SNR was an important metric in assessing uncertainty in the data. The SNR was defined as the ratio of the peak signal divided by the standard deviation of the noise. Typically, any trace with a SNR of less than 3 was considered to be statistically insignificant. At this value of SNR, any peak present was barely detectable against the noise. Since three injection axes were used, if the SNR was low on one axis, an averaged velocity vector could still be calculated from the remaining two axes. Where reliable data was available from all three axes, calculations of the axial velocity were performed using different combination of axes to help assess the uncertainties in the calculated velocities. An assessment of more than 300 data points across various operating conditions showed that the uncertainties were typically within ±100 m/s but could rise to as high as ±600 m/s for peaks with low SNR (SNR just high enough to make out the presence of the peak). The uncertainty from the wavemeter and optogalvanic cell combination was ±50 m/s and is much lower than the uncertainty from the noise. Scanning resolution of the laser was set sufficiently fine so as not to contribute to the total uncertainty. The effective total uncertainty was ±112 m/s for most scans and up to ±600 m/s for scans with low SNR.

IV. Results

A. Axial Variation in Acceleration Profile

Figure 8 shows the averaged axial velocity as a function of position along the discharge channel centerline for the tested magnetic field configurations with the thruster operating at 300 V, 6.3 kW. Figure 9 shows the same for 600 V, 12.5 kW operations.

Recall that the location of peak radial magnetic field moves axially by roughly the same amount between each configuration in the series. Figure 8 and Figure 9 shows the overall shape of the acceleration profile was maintained across magnetic field configuration but the location shifts upstream with increasing B number. Furthermore, there is a clear jump in the location of the acceleration zone between B1 and B2. Modeling work described in an earlier publication points to a possible explanation for this behavior.[22] For B0 and B1, the acceleration zone plasma, which is characterized by energetic electrons, were anchored to the downstream facing surfaces at the edge of the pole covers while for B2 and B4 the same plasma were anchored to the discharge channel walls. Figure 10 shows a reproduction of Hall2De simulations from the earlier publication for convenience.[22] Figure 10 illustrates the difference in plasma attachment locations between B1
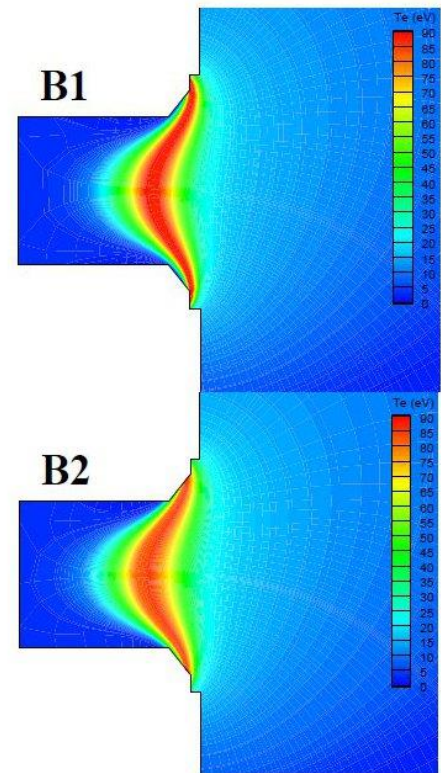

Figure 10. Hall2De simulations reproduced from prior publication for to aid in visualization of plasma attachment locations.[22]

and B2. This is not to say that for B1 there were no plasma bombarding the channel walls or that for B2 there were no plasma bombarding the pole cover surfaces. Instead, the hypothesis is that the ratio of plasma bombarding the pole cover surfaces versus the channel walls underwent a drastic change between B1 and B2. When the energetic part of the plasma is preferentially attaching to the edge of the pole covers, the plasma geometry is associated with magnetic shielding. When the energetic part of the plasma is preferentially attaching to the discharge channel walls, the plasma geometry is associated with reduced or no shielding.

LIF data taken along discharge channel centerline, like what is shown here, can potentially be used to empirically determine when a thruster magnetic field configuration is fully magnetically shielded. However, it should be mentioned that a particular Hall thruster may not require full magnetic shielding to achieve desired wear life. One of the values of the magnetic optimization test is to demonstrate that Hall thruster designers can trade discharge channel wear against pole cover wear.
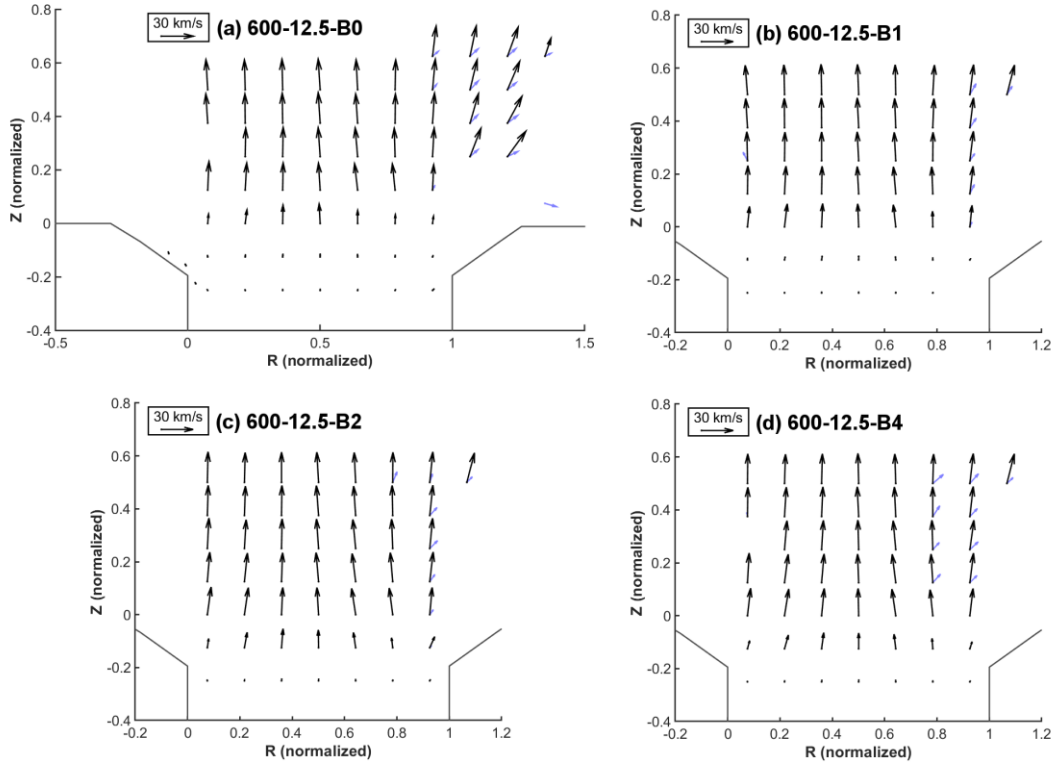
B. Variation in Acceleration Characteristics in the Discharge Channel

Figure 11 shows the averaged velocity vector in and near the discharge channel for 300 V, 6.3 kW operations with different magnetic field configurations. Figure 12 shows the same for 600 V, 12.5 kW operations. Subplot (a) to (d) of each figure corresponds to configuration B0, B1, B2, and B4, respectively. In each subplot, the black arrows represents the velocity vectors of the beam ions while the blue arrows represents the velocity vectors of the low energy ions. While the low energy ions were likely present throughout the radial edges of each map, SNR was not high enough at all locations for the low energy populations to be detected. The locations with blue arrows are the locations where the low energy populations could be definitively identified.
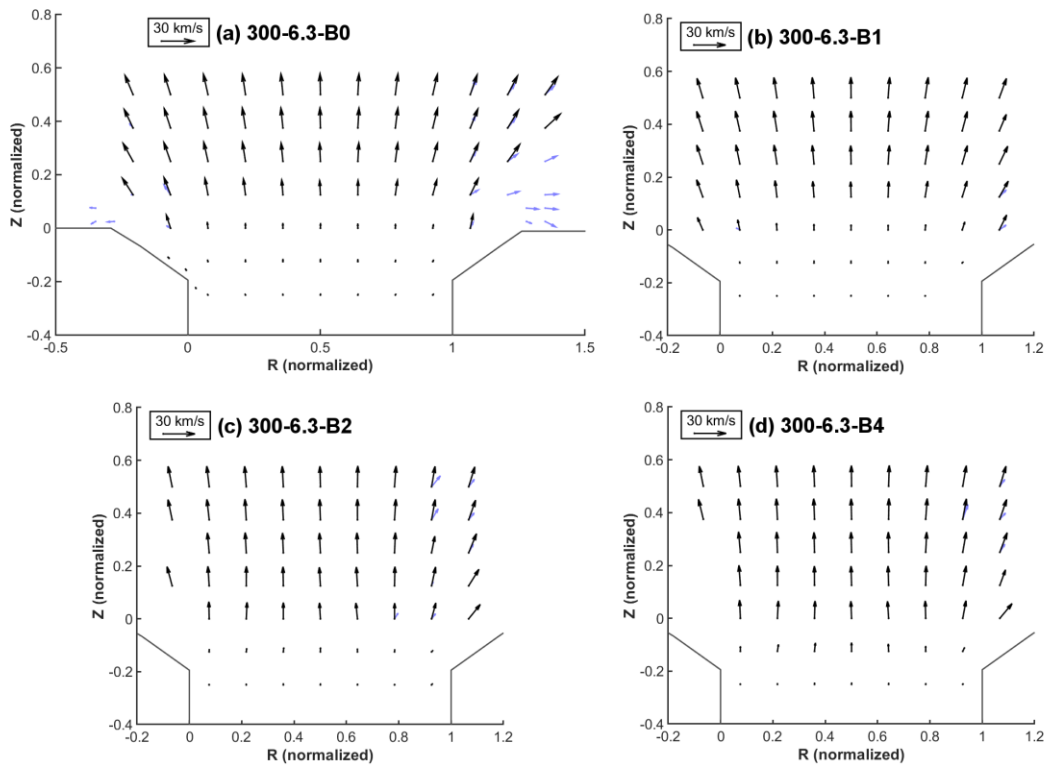
Figure 11. Averaged ion velocity vector in and near the discharge channel for 300 V, 6.3 kW operations with different magnetic field configurations.
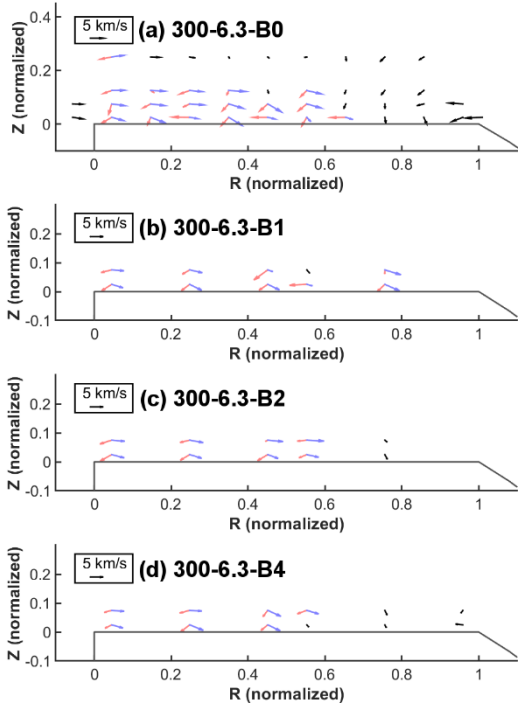
Figure 12. Averaged ion velocity vector in and near the discharge channel for 600 V, 12.5 kW operations with different magnetic field configurations.

From Figure 11 and Figure 12, one can see trends in the velocity vectors as the magnetic field moved upstream. The acceleration moved upstream as the magnetic field moved but there was a large jump in this movement between B1 and B2. One can see this by comparing Figure 11 subplot (b) with subplot (c). Whereas the third from the bottom row of vectors have low velocities in subplot (b), they have much higher velocities in subplot (c). A similar comparison can be made between Figure 12 subplot (b) and subplot (c) by looking at the second from the bottom row of vectors.

Another trend in Figure 11 and Figure 12 is that the divergence of the vectors are slightly smaller when going from B1 to B2. There is a noticeable change in the velocity vector where all the vectors along the acceleration zone points slightly more inward, towards the channel centerline, for B2 than for B1. This trend is in agreement with past work that showed the divergence of magnetically shielded thrusters are slightly larger than the divergence of non-shielded thruster. This evidence support the hypothesis that B1 was magnetically shielded while B2 corresponded to reduced shielding.

C. Variation in Ion Characteristics near the Front Poles

Figure 13 shows the averaged ion velocity vectors near the inner front pole cover (IFPC) for 300 V, 6.3 kW operations with different magnetic field configurations. Figure 14 shows the same for 600 V, 12.5 kW operations. Subplot (a) to (d) of each figure corresponds to configuration B0, B1, B2, and B4, respectively. In each figure, the blue arrows corresponded to the cathode stream while the red arrows corresponded to the discharge channel stream. Black arrows were used when the two ion populations near the IFPC could not be separated either due to low SNR or one population being much more dominant than the other.

Figure 13. Averaged ion velocity vector near the inner front pole cover for the TDU1 operating at 300 V, 6.3 kW with different magnetic field configurations.
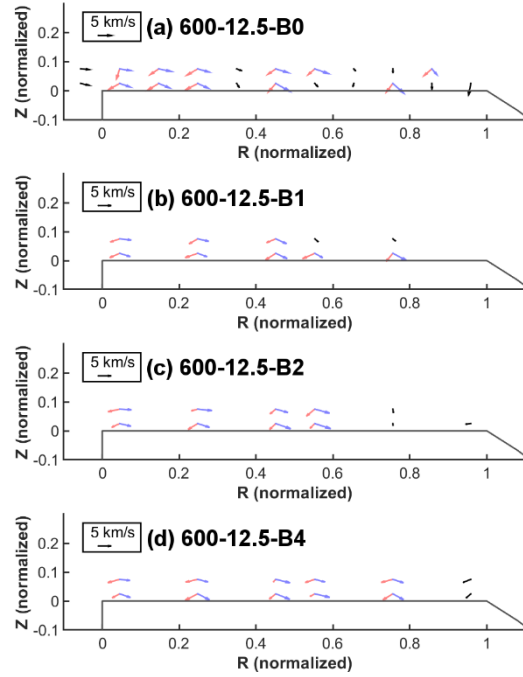
Figure 14. Averaged ion velocity vector near the inner front pole cover for the TDU1 operating at 600 V, 12.5 kW with different magnetic field configurations.

From the locations where the two ion populations were successfully separated, the ion characteristics were averaged. This averaging improves the statistical significance of the averaged value at cost of spatial details. Table 2 summarizes the directed ion energy, FWHM energy, and angle of incidence (AOI) with respect to the IFPC macro surface normal. The directed ion energy was the magnitude of the averaged velocity converted to energy. The FWHM energy was the width of the energy distribution function as derived from the VDF measured at half of maximum intensity. This parameter was a simple way of describing the range of energies that the ions had. The majority of the ions would have energies within one FWHM energy of the mean. However, a few percent of the distribution have energies higher than one FWHM. The FWHM energy was provided here as a guide and not an absolute indicator. Uncertainties are based on 95% confidence.

**Table 2. Ion characteristics near the IFPC.**

Operating Condition	Sample Size	Discharge Channel Stream			Cathode Stream		
		Directed energy, eV	FWHM energy, eV	Averaged AOI, degree	Directed energy, eV	FWHM energy, eV	Averaged AOI, degree
300-6.3-B0	13	17 ±3	30 ±4	48 ±15	18 ±5	42 ±9	66 ±8
300-6.3-B1	9	17 ±7	30 ±3	49 ±15	17 ±6	36 ±7	67 ±6
300-6.3-B2	8	12 ±4	29 ±7	62 ±8	19 ±4	46 ±10	75 ±6
300-6.3-B4	7	10 ±3	20 ±6	54 ±11	19 ±3	40 ±6	69 ±9
600-12.5-B0	11	16 ±2	28 ±6	43 ±8	18 ±4	38 ±4	61 ±8
600-12.5-B1	8	15 ±3	27 ±7	56 ±8	16 ±4	39 ±4	64 ±7
600-12.5-B2	8	11 ±3	31 ±7	51 ±10	21 ±4	39 ±4	72 ±5
600-12.5-B4	10	12 ±4	30 ±5	57 ±8	17 ±3	33 ±4	67 ±5

From Table 2, one can see that the characteristics were very similar between B0 and B1, as well as between B2 and B4. Directed energy of the ions were slightly reduced when going from configuration B1 to B2 but the difference in energy was close to the measurement uncertainty of the LIF diagnostic. Thus, one could state that the

ion energy characteristics for all four configuration were very similar. AOI of the ions in the discharge channel stream appeared to have increased slightly as one goes from B0 to B4. AOI of the cathode stream was largely similar across the four configurations.

Figure 15 shows the averaged ion velocity vectors near the outer front pole cover (OFPC) for 300 V, 6.3 kW operations with different magnetic field configurations. Figure 16 shows the same for 600 V, 12.5 kW operations. Subplot (a) to (d) of each figure corresponds to configuration B0, B1, B2, and B4, respectively. SNR tended to be low for OFPC locations and was lower for some operating conditions than others. In particular, SNR decreased noticeably when going from B1 to B2 for 300 V, 6.3 kW operations but increased when going from B1 to B2 for 600 V, 12.5 kW operations.

Ion energies near the OFPC appeared to decrease when going from B0 to B4. The vector arrows were shorter for B2 and B4 than for B0 and B1. However, due to low SNR, the statistical significance of this trend was limited.
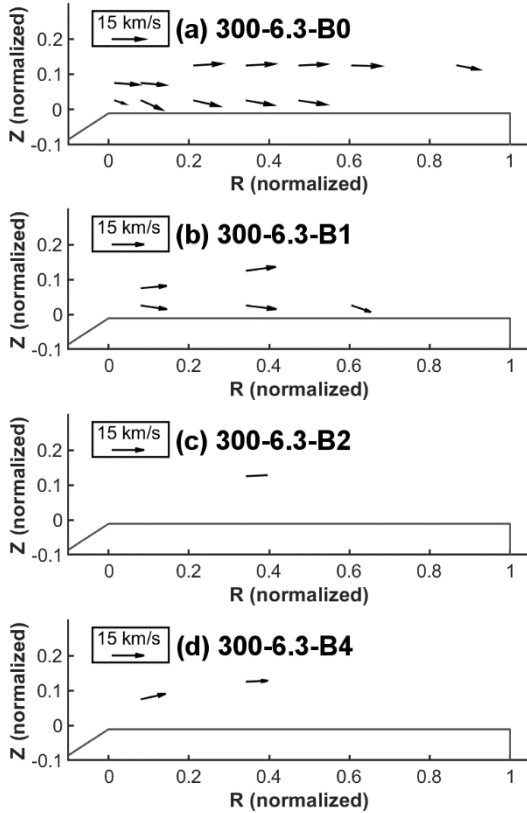
Figure 15. Averaged ion velocity vector near the outer front pole cover for the TDU1 operating at 300 V, 6.3 kW with different magnetic field configurations.
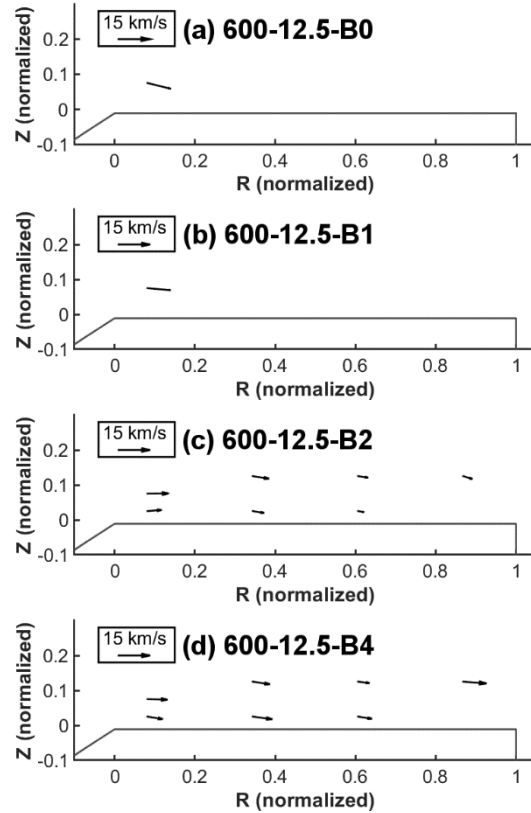
Figure 16. Averaged ion velocity vector near the outer front pole cover for the TDU1 operating at 600 V, 12.5 kW with different magnetic field configurations.

V. Conclusions

LIF diagnostic was successfully deployed in the magnetic optimization test of the HERMeS TDU1. During this test, the acceleration zone was observed to undergo a major shift when going from the magnetic configuration B1 to B2. Much smaller shifts were found when going from B0 to B1 and from B2 to B4. The data and prior simulation works suggest the energetic portion of the discharge plasma switched from preferentially anchoring to the poles for B0 and B1 to preferentially anchoring to the channel wall for B2 and B4. This trend suggested the possibility that different plasma-wall interaction physics applies to a magnetically shielded thruster than a non-shielded thruster.

Averaged ion velocity vector maps from the discharge channel confirms the large shift in acceleration zone between B1 and B2. These maps also confirmed that B0 and B1 were more like magnetically shielded configuration while B2 and B4 were more like non-shielded configuration.

Examination of the data near the inner front pole cover showed that the ion energy characteristics were largely the same across configurations. Similar examination of the data near the outer front pole cover showed a decrease in ion energy as one goes from B0 to B4. However, only a limited amount of OFPC data could be collected.

Acknowledgments

References

[1]Smith, B. K., Nazario, M. L., and Cunningham, C. C., "Solar Electric Propulsion Vehicle Demonstration to Support Future Space Exploration Missions", *Space Propulsion 2012*, Bordeaux, France, May 7-10, 2012.

[2]Congress, "National Aeronautics and Space Administration Transition Authorization Act of 2017", 2017.

[3]NASA HQ, "Meeting Agenda and Minutes", https://www.nasa.gov/sites/default/files/atoms/files/nac_heoc_march_2017_public_agenda_revb.pdf, 2017.

[4]Gerstenmaier, W., "Progress in Defining the Deep Space Gateway and Transport Plan", https://www.nasa.gov/sites/default/files/atoms/files/nss_chart_v23.pdf, 2017.

[5]Manzella, D. H. and Hack, K., "High-Power Solar Electric Propulsion for Future NASA Missions", *50th AIAA/ASME/SAE/ASEE Joint Propulsion Conference*, AIAA-2014-3718, doi:10.2514/6.2014-3718, Cleveland, OH, Jul 28-30, 2014.

[6]Herman, D. A., et al., "Overview of the Development and Mission Application of the Advanced Electric Propulsion System (AEPS)", *35th International Electric Propulsion Conference*, 2017-284, Atlanta, GA, Oct 8-12, 2017.

[7]Hofer, R. R., et al., "Development Status of the 12.5 kW Hall Effect Rocket with Magnetic Shielding (HERMeS)", *35th International Electric Propulsion Conference*, 2017-231, Atlanta, GA, Oct 8-12, 2017.

[8]Huang, W., Yim, J. T., and Kamhawi, H., "Design and Empirical Assessment of the HERMeS Hall Thruster Propellant Manifold", *62nd Joint Army-Navy-NASA-Air Force Propulsion Meeting*, JANNAF-2015-3926, Nashville, TN, Jun 1-4, 2015.

[9]Shastry, R., Huang, W., and Kamhawi, H., "Near-Surface Plasma Characterization of the 12.5-kW NASA TDU1 Hall Thruster", *51st AIAA/ASME/SAE/ASEE Joint Propulsion Conference*, AIAA-2015-3919, doi:10.2514/6.2015-3919, Orlando, FL, Jul 27-29, 2015.

[10]Kamhawi, H., et al., "Performance and Facility Background Pressure Characterization Tests of NASA's 12.5-kW Hall Effect Rocket with Magnetic Shielding Thruster", *34th International Electric Propulsion Conference*, 2015-007, Kobe, Japan, Jul 4-10, 2015.

[11]Huang, W., Kamhawi, H., and Haag, T. W., "Plasma Oscillation Characterization of NASA's HERMeS Hall Thruster via High Speed Imaging", *52nd AIAA/ASME/SAE/ASEE Joint Propulsion Conference*, AIAA-2016-4829, doi:10.2514/6.2016-4829, Salt Lake City, UT, Jul 25-27, 2016.

[12]Kamhawi, H., et al., "Performance, Facility Pressure Effects, and Stability Characterization Tests of NASA's Hall Effect Rocket with Magnetic Shielding Thruster", *52nd AIAA/ASME/SAE/ASEE Joint Propulsion Conference*, AIAA-2016-4826, doi:10.2514/6.2016-4826, Salt Lake City, UT, Jul 25-27, 2016.

[13]Huang, W., Kamhawi, H., Myers, J. L., Yim, J. T., and Neff, G., "Non-Contact Thermal Characterization of NASA's HERMeS Hall Thruster", *51st AIAA/ASME/SAE/ASEE Joint Propulsion Conference*, AIAA-2015-3920, doi:10.2514/6.2015-3920, Orlando, FL, Jul 27-29, 2015.

[14]Myers, J. L., Kamhawi, H., Yim, J. T., and Clayman, L., "Hall Thruster Thermal Modeling and Test Data Correlation", *52nd AIAA/ASME/SAE/ASEE Joint Propulsion Conference*, AIAA-2016-4535, doi:10.2514/6.2016-4535, Salt Lake City, UT, Jul 25-27, 2016.

[15]Huang, W., Kamhawi, H., Haag, T. W., Lopez Ortega, A., and Mikellides, I. G., "Facility Effect Characterization Test of NASA's HERMeS Hall Thruster", *52nd AIAA/ASME/SAE/ASEE Joint Propulsion Conference*, AIAA-2016-4828, doi:10.2514/6.2016-4828, Salt Lake City, UT, Jul 25-27, 2016.

[16]Peterson, P. Y., et al., "NASA's HERMeS Hall Thruster Electrical Configuration Characterization ", *52nd AIAA/ASME/SAE/ASEE Joint Propulsion Conference*, AIAA-2016-5027, doi:10.2514/6.2016-5027, Salt Lake City, UT, Jul 25-27, 2016.

[17]Huang, W., et al., "Plasma Plume Characterization of the HERMeS during a 1722-hr Wear Test Campaign", *35th International Electric Propulsion Conference*, 2017-307, Atlanta, GA, Oct 8-12, 2017.

[18]Williams, G. J., et al., "Wear Testing of the HERMeS Thruster", *52nd AIAA/ASME/SAE/ASEE Joint Propulsion Conference*, AIAA-2016-5025, doi:10.2514/6.2016-5025, Salt Lake City, UT, Jul 25-27, 2016.

[19]Williams, G. J., et al., "Wear Trends of the HERMeS Thruster as a Function of Throttle Point", *35th International Electric Propulsion Conference*, 2017-207, Atlanta, GA, Oct 8-12, 2017.

[20]Huang, W., Kamhawi, H., and Herman, D. A., "Ion Velocity in the Discharge Channel and Near-Field of the HERMeS Hall Thruster", *2018 Joint Propulsion Conference*, AIAA-2018-4723, Cincinnati, OH, Jul 9-11, 2018.

[21]Huang, W., Kamhawi, H., and Herman, D. A., "Evidence of Counter-Streaming Ions near the Inner Pole of the HERMeS Hall Thruster", *2019 Joint Propulsion Conference*, AIAA-2019-3897, Indianapolis, IN, Aug 19-22, 2019.

[22]Kamhawi, H., Huang, W., and Mikellides, I. G., "Optimization of the Magnetic Field Topology in the Hall Effect Rocket with Magnetic Shielding", *2018 Joint Propulsion Conference*, AIAA-2018-4720, Cincinnati, OH, Jul 9-11, 2018.

[23]Chaplin, V. H., et al., "Laser Induced Fluorescence Measurements of the Acceleration Zone in the 12.5 kW HERMeS Hall Thruster", *35th International Electric Propulsion Conference*, 2017-229, Atlanta, GA, Oct 8-12, 2017.

[24]Polk, J. E., et al., "Inner Front Pole Erosion in the 12.5 kW HERMeS Hall Thruster Over a Range of Operating Conditions", *35th International Electric Propulsion Conference*, 2017-409, Atlanta, GA, Oct 8-12, 2017.

[25]Lobbia, R. B., Conversano, R. W., Reilly, S., Hofer, R. R., and Sorensen, R., "Environmental Testing of the HERMeS TDU-2 Hall Thruster", *2018 Joint Propulsion Conference*, AIAA-2018-4646, Cincinnati, OH, Jul 9-11, 2018.

[26]Chaplin, V. H., et al., "Spatiotemporally Resolved Ion Velocity Distribution Measurements in the 12.5 kW HERMeS Hall Thruster", *36th International Electric Propulsion Conference*, 2019-532, Vienna, Austria, Sep 15-20, 2019.

[27]Kamhawi, H., et al., "Performance, Stability, and Plume Characterization of the HERMeS Thruster with Boron Nitride Silica Composite Discharge Channel", *35th International Electric Propulsion Conference*, 2017-392, Atlanta, GA, Oct 8-12, 2017.

[28]Frieman, J. D., et al., "Long Duration Wear Test of the NASA HERMeS Hall Thruster", *2018 Joint Propulsion Conference*, AIAA-2018-4645, Cincinnati, OH, Jul 9-11, 2018.

[29]Frieman, J. D., et al., "Completion of the Long Duration Wear Test of the NASA HERMeS Hall Thruster", *2019 Joint Propulsion Conference*, AIAA-2019-3895, Indianapolis, IN, Aug 19-22, 2019.

[30]Peterson, P. Y., et al., "Reconfiguration of NASA GRC's Vacuum Facility 6 for Testing of Advanced Electric Propulsion System (AEPS) Hardware", *35th International Electric Propulsion Conference*, 2017-028, Atlanta, GA, Oct 8-12, 2017.

[31]Yim, J. T. and Burt, J. M., "Characterization of Vacuum Facility Background Gas Through Simulation and Considerations for Electric Propulsion Ground Testing", *51st AIAA/ASME/SAE/ASEE Joint Propulsion Conference*, AIAA-2015-3825, doi:10.2514/6.2015-3825, Orlando, FL, Jul 27-29, 2015.

[32]Huang, W., Smith, T. B., and Gallimore, A. D., "Obtaining Velocity Distribution using a Xenon Ion Line with Unknown Hyperfine Constants", *40th AIAA Plasmadynamics and Laser Conference*, AIAA-2009-4226, doi:10.2514/6.2009-4226, San Antonio, Texas, Jun 22-25, 2009.

[33]Huang, W., *Singly-Charged Xenon Zeeman Effect Study Results and Validation*, in *Study of Hall Thruster Discharge Channel Wall Erosion via Optical Diagnostics*, University of Michigan, Ann Arbor, MI, 2011, pp. 59-62.

[34]Huang, W., Drenkow, B., and Gallimore, A. D., "Laser-Induced Fluorescence of Singly-Charged Xenon Inside a 6-kW Hall Thruster", *45th AIAA/ASME/SAE/ASEE Joint Propulsion Conference & Exhibit*, AIAA-2009-5355, doi:10.2514/6.2009-5355, Denver, CO, Aug 2-5, 2009.